

Sink of Eddy Energy by Submesoscale Sea Surface Temperature Variability in a Coupled Regional Model

IGOR UCHOA^a, JACOB WENEGRAT,^a AND LIONEL RENAULT^b

^a Department of Atmospheric and Oceanic Science, University of Maryland, College Park, College Park, Maryland
^b LEGOS, University of Toulouse, IRD, CNRS, CNES, UPS, Toulouse, France

(Manuscript received 15 March 2024, in final form 13 March 2025, accepted 1 April 2025)

ABSTRACT: Air-sea interaction impacts ocean energetics via modifications to the exchange of momentum and buoyancy. Prior work at the submesoscale has largely focused on mechanisms related to the eddy kinetic energy (EKE), such as the current feedback on stress, which generates negative wind work, or variations in sea surface temperature (SST) that modify surface winds. However, less is known about the influence of submesoscale SST variability on ocean energetics through its direct effect on the surface flux of available potential energy. In this work, the role of air-sea fluxes on submesoscale ocean energetics is investigated using a fully coupled model of the California Current region, including a numerical experiment that suppresses the thermal response in the computation of air-sea fluxes at the submesoscale. Correlations between surface buoyancy anomalies and surface buoyancy fluxes lead to an approximately 10%–20% loss of submesoscale eddy potential energy (EPE), which results in similar magnitude reductions of the vertical buoyancy production, EKE, and eddy wind work. The changes induced by this mechanism in the energy reservoirs and dissipation/conversion pathways are on the same order of magnitude as the negative wind work induced by the current feedback. A scaling for the EPE flux shows that it is a function of the density ratio and proportional to the surface EPE reservoir of the system. These findings indicate the importance of the submesoscale SST variability and small-scale variability in surface heat fluxes in modifying energy reservoirs and conversion pathways of the ocean via the direct flux of EPE at the air-sea interface.

SIGNIFICANCE STATEMENT: This work investigates the impact of small oceanic frontal features in the ocean, classified as submesoscale, on the exchange of energy at the air-sea boundary. Submesoscale fronts and filaments range from approximately 0.1–10 km and are characterized by strong horizontal density changes and fast-evolving flow. The associated density anomalies at the surface may be important in the overall energy budget of the surface ocean since they can affect the energy fluxes at the air-sea boundary. Two numerical experiments were set up for a comparative analysis of the energy transfer, conversion, and storage in the upper layer of the California Current region. One simulation works as a control experiment with air-sea fluxes calculated using the full-resolution fields. In the second experiment, the role of sea surface temperature anomalies in generating air-sea fluxes is suppressed. A comparison between the two experiments shows a difference of 10%–20% in the energy storage and conversion. Sea surface temperature variability may induce a reduction of energy via air-sea fluxes similar to energy dissipation driven by wind-current interactions on the same scale of phenomena.

KEYWORDS: Atmosphere-ocean interaction; Energy transport; Sea surface temperature; Heat budgets/fluxes; Ocean models

1. Introduction

The turbulent heat and momentum exchanges across the ocean-atmosphere interface are intrinsically dependent on the scale of the ocean features (Seo et al. 2023). Sea surface temperature (SST) variability at the mesoscale plays an essential role in modifying the overlaying atmospheric dynamics, which in turn leads to substantial coupled responses of the ocean (Bishop et al. 2017; Chelton and Xie 2010; O'Neill et al. 2012; Small et al. 2008). However, much of our understanding of how ocean variability leads to coupled interactions is constrained to mesoscale resolution (10–100 km). At smaller scales in the ocean, frontal and filamentous features on the order of 0.1–10 km—denoted submesoscale—are characterized by sharper temperature gradients and ageostrophic flows.

Submesoscale currents are common oceanic features driven by the downscale eddy cascade of mesoscale flows and are important to global ocean dynamics (McWilliams 2016; Wenegrat et al. 2018). As the dynamics of submesoscale currents are strongly ageostrophic, strong vertical velocities are characteristic in the flow, which allow for significant transport of properties such as dissolved gases, nutrients, and heat (Mahadevan et al. 2012; Renault et al. 2016; Balwada et al. 2021). The vertical flux of heat (buoyancy) affects both the timing and strength of ocean stratification (Mahadevan et al. 2012; Johnson et al. 2016) and the surface flux of heat between the ocean and the atmosphere (Su et al. 2018, 2020; Iyer et al. 2022).

Air-sea interaction at the submesoscale is somewhat less well understood since numerical simulations are computationally costly and observations are challenging. Observations of air-sea fluxes at the submesoscale, although scarce, have shown larger fluxes of heat, moisture, and momentum at fronts (Shao et al. 2019; Iyer et al. 2022), also consistent with

Corresponding author: Igor Uchoa, iufarias@umd.edu

submesoscale-permitting global ocean model analyses that used uncoupled air-sea bulk formulas (e.g., Su et al. 2018, 2020). Coupled numerical simulations have shown an active eddy kinetic energy (EKE) transfer at the air-sea interface by submesoscale variations in surface wind stress (e.g., Renault et al. 2018; Bai et al. 2023; Conejero et al. 2024). For example, coupled modeling experiments of the California Current System indicate that modifications to the wind stress by small-scale currents (the current feedback (CFB) on stress) lead to a 17% reduction in submesoscale EKE (Renault et al. 2018). These changes to the surface stress also modify the Ekman transport of buoyancy at fronts and, consequently, the PV budget of the surface mixed layer (Wenegrat 2023). In addition, modulations of the marine atmospheric boundary layer and changes in atmospheric kinetic energy by SST variability, namely, the thermal feedback (TFB) mechanism, were also explored in idealized models (Wenegrat and Arthur 2018; Sullivan et al. 2020, 2021). These results indicate that sharp fronts at the submesoscale impact the response of the marine atmospheric boundary layer by driving secondary circulations in the atmosphere, which in turn modify the surface wind stress and wind work (Skillingstad et al. 2007; Wenegrat and Arthur 2018; Sullivan et al. 2021). Recent studies also show the combined effect of CFB and TFB on the wind stress (Bai et al. 2023; Conejero et al. 2024), which indicates that submesoscale SST variability shows a direct influence on the transfer of momentum between the atmosphere and the ocean, modifying the surface flux of EKE.

The influence of submesoscale SST variability on ocean energetics through its direct effect on the surface flux of available potential energy (APE), however, is less explored. Observations show strong covariability between surface heat fluxes and surface buoyancy anomalies at the submesoscale (Shao et al. 2019; Iyer et al. 2022; Yang et al. 2024), suggesting there will also be a direct surface flux of submesoscale APE. Using an approximate formulation of APE, i.e., eddy potential energy (EPE, discussed further below), studies have shown that air-sea fluxes contribute to a sink of EPE at the mesoscale (Bishop et al. 2020; Guo et al. 2022), which impacts the baroclinic conversion rate in boundary currents in the first 100 m of the upper ocean (Ma et al. 2016; Renault et al. 2023). However, similar analyses have not yet been explored using submesoscale-permitting models. Here, we investigate the impact of SST anomalies on submesoscale APE flux using a fully coupled regional model of a portion of the California Current System, a region where submesoscale features have been indicated as important drivers of air-sea fluxes of momentum and heat (Capet et al. 2008b; Renault et al. 2018).

Two coupled ocean-atmosphere simulation setups are used to assess the effect of submesoscale SST variability on the APE flux, including both a fully coupled simulation and one in which submesoscale SST anomalies are not included for air-sea flux calculations. The flux, conversion, and storage components of eddy energy in the mixed layer for both simulations are compared, highlighting an increase of eddy energy when SST anomalies do not affect surface fluxes. The impact of the surface APE flux is not limited to the EPE reservoir but also propagates to changes in EKE through modification of the vertical buoyancy production and changes to the surface wind work. This analysis shows that the flux of APE driven by SST at the

submesoscale is comparable in magnitude and effect to analogous transfers of EKE by surface momentum transfer (wind work) at the submesoscale.

The work is organized as follows. Section 2 introduces the theoretical background for the eddy energy reservoirs, conversion rates, and fluxes in spectral space and their appropriate approximations. The numerical experiments are described in section 3. In section 4, the submesoscale dynamics of the numerical simulations are described, and the impact of the surface EPE flux is estimated. An approximated form of the EPE flux is obtained and compared with the flux of EKE by the surface wind work in section 5. Finally, the results are summarized in section 6.

2. Definition of energy terms

This work compares the eddy energy pathways and reservoirs of the upper ocean, assessing the influence of submesoscale SST anomalies on air-sea flux variability. We consider the reservoirs, conversion rates, and flux terms of eddy energy in horizontal wavenumber space. The definition of global APE describes this quantity as a volume-conserved subtraction of a background state of minimal energy from the total potential energy of the fluid (Winters et al. 1995). However, if one is interested in the spatial distribution of APE, the local formulation is suited (Roulet and Klein 2009; Winters and Barkan 2013; Zemskova et al. 2015). The local APE per unit density is defined as

$$\text{APE} = - \int_{z_r(b)}^z [b - b_r(z')] dz', \quad (1)$$

where $b = -g[(\rho - \rho_o)/\rho_o]$ is the local buoyancy of the fluid, g is the gravitational acceleration, and ρ_o is the background surface density. The subscript r denotes a reference buoyancy profile calculated by spatially resorting density ρ_r to a minimal potential energy state, and z_r represents the equilibrium depth of a water parcel of buoyancy b with respect to b_r (Tseng and Ferziger 2001; Huang 2005; Stewart et al. 2014).

A first-order approximation of (1) can be applied if the displacements between the water parcels and their equilibrium height, namely, $z - z_r$, are sufficiently small and the local reference profile is approximately linear (Molemaker and McWilliams 2010; Roulet and Klein 2009). This approximate form is often referred to as the quasigeostrophic limit (Lorenz 1955; von Storch et al. 2012; Stewart et al. 2014), and it is described as follows:

$$\text{APE} \approx \frac{1}{2} \frac{[b - b_r]^2}{N_r^2}, \quad (2)$$

where $N_r^2 = \partial b_r / \partial z$ is the reference squared Brunt-Väisälä frequency. This approximate form—which we refer to as the EPE for clarity of terminology—has been used previously for studying both the mesoscale (e.g., Ma et al. 2016; Bishop et al. 2020; Guo et al. 2022) and submesoscale dynamics of the upper ocean (e.g., Callies and Ferrari 2013; Callies et al. 2015; Cao et al. 2021; Yang et al. 2021), and we use it in several

places throughout the manuscript (for derivation of the EPE budget, see von Storch et al. 2012). More details on this formulation of the EPE, as well as the validity of the approximation, are provided in appendix A.

The reservoirs of EPE and EKE in spectral space are described as follows:

$$\text{EPE} = \mathbb{R}\left[\frac{(\widehat{b} - \widehat{b}_r)(\widehat{b} - \widehat{b}_r)^*}{2N_r^2}\right], \quad (3)$$

$$\text{EKE} = \mathbb{R}\left[\frac{\widehat{u}\widehat{u}^* + \widehat{v}\widehat{v}^*}{2}\right], \quad (4)$$

where u and v are the zonal and meridional velocity components. The caret ($\widehat{\cdot}$) denotes the two-dimensional Fourier transform. The symbol \mathbb{R} represents the real component of the spectra, and the asterisk (*) indicates the complex conjugate operator. The eddy terms analyzed in this work refer to the variability encompassed at the small mesoscale and submesoscale horizontal wavenumbers (see section 3c).

The rate of conversion between EPE and EKE, $C_{(\text{EKE}, \text{EPE})}$, is

$$C_{(\text{EKE}, \text{EPE})} = \mathbb{R}\{\widehat{w}(\widehat{b} - \widehat{b}_r)^*\}, \quad (5)$$

where w represents the vertical velocity component. Conversion of EPE at the submesoscale is generated by baroclinic mixed-layer instabilities and other ageostrophic secondary circulations that extract available potential energy from fronts (Fox-Kemper et al. 2008; Wenegrat and McPhaden 2016).

APE can be fluxed at the surface when there are correlations between surface buoyancy fluxes and the reference depth (Scotti and White 2014; Hogg et al. 2013; Zemskova et al. 2015):

$$G_{\text{APE}} = -\mathbb{R}[\widehat{z}_{r_o}^* \widehat{B}_o], \quad (6)$$

where z_{r_o} is the equilibrium height of the surface buoyancy and B_o is the net surface buoyancy flux (defined as positive when into the ocean). The EPE flux likewise takes a similar form (von Storch et al. 2012):

$$G_{\text{EPE}} = \mathbb{R}\left[\frac{(\widehat{b}_o - \widehat{b}_{r_o})^* \widehat{B}_o}{N_r^2}\right], \quad (7)$$

where b_o and b_{r_o} are the surface buoyancy and surface reference buoyancy, respectively. Negative $G_{\text{APE/EPE}}$ values indicate APE/EPE loss from the ocean, whereas positive $G_{\text{APE/EPE}}$ values indicate a gain of APE/EPE.

Analogously, the flux of EKE at the surface (or wind work) may be calculated using the surface boundary conditions for momentum (see Capet et al. 2008b; von Storch et al. 2012). The wind work G_{EKE} is thus defined as

$$G_{\text{EKE}} = \frac{1}{\rho_o} (\mathbb{R}[\widehat{\tau}_x \widehat{u}_o^* + \widehat{\tau}_y \widehat{v}_o^*]), \quad (8)$$

where $\boldsymbol{\tau} = (\tau_x, \tau_y)$ is the surface momentum flux vector and $\mathbf{u}_o = (u_o, v_o)$ is the surface velocity vector.

3. Numerical simulation

a. Model description

The ocean components of the coupled model in the California Current System region use the Regional Ocean Modeling System (ROMS) in its Coastal and Regional Ocean Community (CROCO) version (Shchepetkin and McWilliams 2005; Debreu et al. 2012; Shchepetkin 2015). CROCO is a free-surface, terrain-following coordinate model with split-explicit time stepping. The equations solved in this model's configurations were set for Boussinesq and hydrostatic approximations. The numerical experiments used in this work are the highest-resolution products from a four-nest configuration described in Renault et al. (2018). The domain for the simulations covers from 119.9° to 128.98°W and from 32.54° to 40.73°N (Fig. 1). The simulations were spun up from the same initial state from June to November 2011, after which they were run separately from November 2011 to June 2012 (more detailed description in section 3b). The boundary and initial conditions are taken from a coarser 4-km nested grid. For the horizontal grid, 1000×1520 points with a grid spacing of $(\Delta x, \Delta y) = 0.5\text{km}$ were set with 80 terrain-and surface-following sigma levels in the vertical with stretching parameters $h_{\text{cline}} = 200\text{m}$, $\theta_b = 3.0$, and $\theta_s = 6$. The turbulence closure used is the K -profile parameterization (KPP; Large et al. 1994). The outputs used in this work are instantaneous fields with 6-h resolution, and the time period analyzed spans a total of 6 months (January–June 2012). More information about the settings and spinup of the model can be found in Renault et al. (2018).

For the atmospheric component of the fully coupled system, the Weather Research and Forecasting (WRF, version 4.1) Model was used (Skamarock et al. 2019). An implementation of a nesting grid is also used in this model as in Renault et al. (2018). The atmospheric component used in this work has a spatial resolution of 2 km with initial and boundary conditions provided by the simulation from the previous nesting with a 6-km horizontal resolution. The domain for the simulations covers from 118.98° to 129.14°W and from 32.44° to 41.20°N, which is slightly larger than the ocean domain to avoid the WRF sponge boundaries. For the horizontal grid, 300×390 points with a grid spacing of $(\Delta x, \Delta y) = 2\text{ km}$ were set with 50 vertical levels. In the boundary layer model, bulk formulas (COARE formulation; Edson et al. 2013) are used to compute the surface turbulent heat, freshwater, and momentum fluxes, which are subsequently provided to CROCO. Note that the implementation of a surface-layer vertical mixing parameterization for the planetary boundary layer (i.e., MYNN; Nakanishi and Niino 2006) and a tridiagonal matrix for vertical turbulent diffusion is necessary for the implementation of relative winds in the atmospheric model and to reproduce the CFB mechanism appropriately (Renault et al. 2019).

The OASIS3 software was used for the surface data exchange between the two models (Valcke 2013) to couple CROCO and WRF. This procedure supports the communication of two-dimensional fields between the two numerical codes for the integration of the coupled system. The diagram in Fig. 2 illustrates the surface fluxes computation using this software. In these experiments, WRF provides the hourly averages of

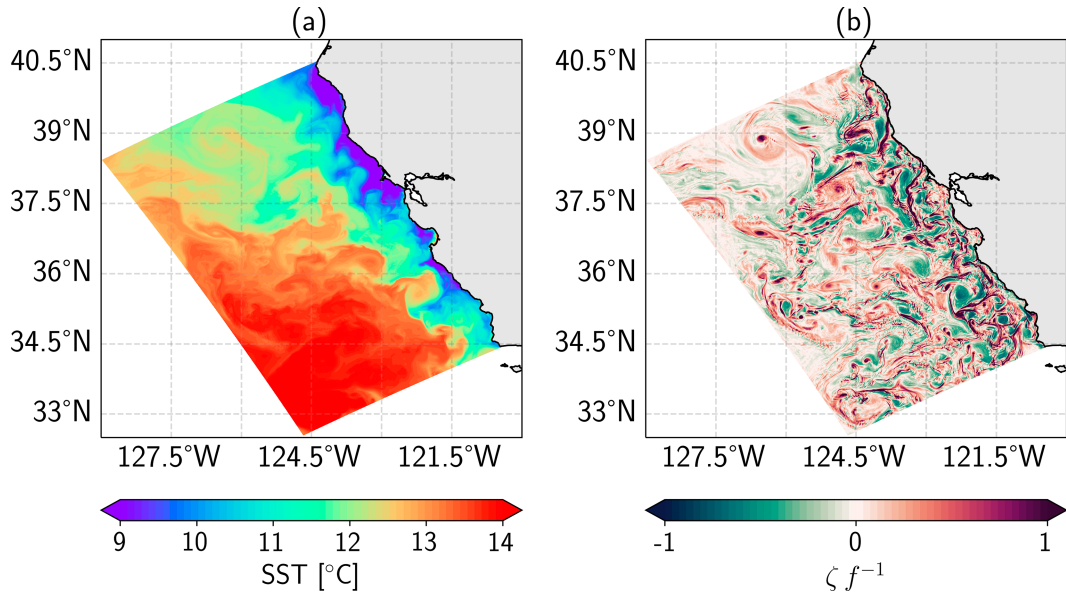


FIG. 1. Snapshots of (a) SST and (b) surface vorticity normalized by the Coriolis frequency f from the fully coupled simulation illustrating the model domain.

freshwater, heat, and momentum fluxes to CROCO, whereas CROCO feeds the hourly SST and surface currents to WRF for the calculation of the fluxes. OASIS3 is implemented in the 4- and 6-km grids for CROCO and WRF, respectively, and nested into the higher-resolution grids.

b. Experiment setup

To observe the impacts of SST variability at the submesoscale on the upper-ocean dynamics, two fully coupled numerical simulations were implemented using two different air-sea coupling configurations. A schematic of the two experimental setups is illustrated in Fig. 2. The first experiment consists of a fully coupled model system, hereafter referred to as the FULL experiment. In the second experiment, SST anomalies are low-pass filtered before being passed to WRF for the calculation of surface fluxes, suppressing the role of submesoscale SST variability in air-sea interaction. The latter experiment will be referred to as the SMTH (as in “smooth”) experiment. We emphasize that the model resolution does not change between simulations—the SMTH experiment has the same resolution as FULL (Fig. 2)—the only change is in the resolution of the SST field used in the calculation of surface fluxes. This comparison between experiments thus allows an assessment of the impact of the ocean submesoscale SST variability on the exchange of heat and momentum at the air-sea interface. This analysis is similar to previous studies performed with mesoscale-resolving simulations (Zhai and Greatbatch 2006; Seo et al. 2016; Renault et al. 2023). For more information on the implementation of air-sea coupling in high-resolution models, the reader is referred to Renault et al. (2018, 2019) and Jullien et al. (2020).

c. Spatial filtering and spectral analysis

A two-dimensional spatial Gaussian filter is used to isolate submesoscale anomalies from the mesoscale and large-scale

signals. The filter applies a $(6\sigma + 1)$ window in both horizontal dimensions and has $\sigma = 3$ and a cutoff value of 0.5 as performed in Renault et al. (2023). This configuration allows for an assessment of the impact of SST submesoscale anomalies on the energy fluxes, reservoirs, and conversion rates. In Fig. 3, an example of the differences in the SST field used in the air-sea coupling between simulations is shown. The filter reduces variability from approximately 50-km wavelength (0.02 cycles km^{-1} wavenumber) to smaller scales, such that at 20-km wavelength (0.05 cycles km^{-1} wavenumber), SST variability (as seen in the calculation of surface fluxes) is reduced by an order of magnitude. Here, we refer to the range of scales smaller than the filter’s largest scale (50 km) as “submesoscale.” However, we note that the submesoscale is more accurately defined as a dynamical regime, and hence the definition employed here is only approximate. The Fourier transform calculation in this work includes subtraction of the spatial mean and tapering using a Hanning window. The spectral analysis performed in this work uses instantaneous fields of the ocean variables and 1-h averaged fields of atmospheric variables. A temporal average of the period of the simulations (i.e., 6 months) is applied in all spectra to reduce uncertainty and high-frequency variability differences between the ocean and atmosphere outputs.

4. Results

a. Model characterization

The submesoscale dynamics of the California Current are depicted in Fig. 1, where SST and normalized relative vorticity fields (i.e., Rossby number) show strong variability in the region. Smaller-scale vortices and their associated high normalized relative vorticity, $\text{Ro} \sim \mathcal{O}(1)$, indicate the presence of flows that are dynamically submesoscale, a consequence of mesoscale strain

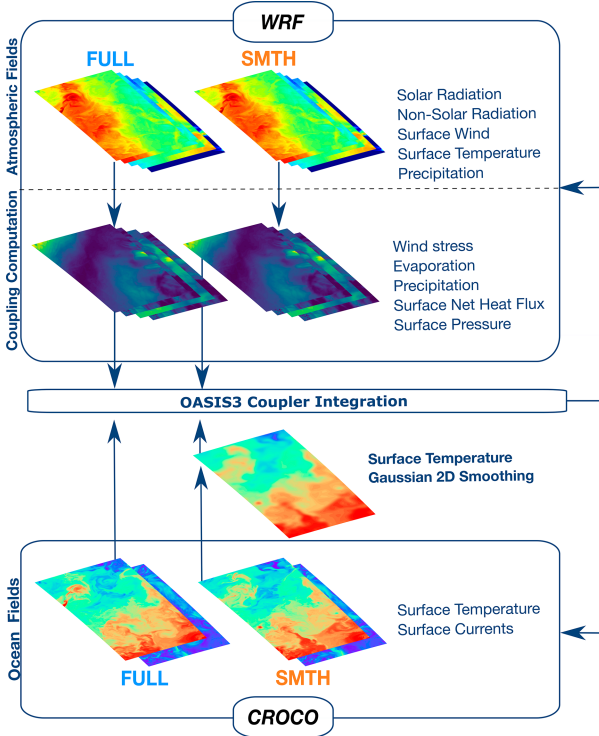


FIG. 2. Schematics of the different coupling computations for the FULL and SMTM experiments using WRF and CROCO. The examples illustrate the computation of the surface fluxes. The filtering of submesoscale SST variability for the coupling computation is illustrated for the SMTM experiment.

and frontal instabilities of the California Current (Capet et al. 2008a).

The surface eddy energy reservoirs, vorticity, and divergence for the two experiments are shown in Fig. 4. The SMTM experiment has approximately 5% more EPE and 10% more EKE than the FULL simulation (Fig. 4a), which suggests an impact from the air-sea fluxes in the surface eddy energy reservoirs. However, the confidence intervals between experiments overlap even though the differences between the spectra are consistent at the submesoscale. Greater differences in energy are found in the fluxes and conversion rates of eddy energy within the mixed layer, as discussed in section 4d. Both EPE and EKE surface spectra have a slope of $\sim k_h^{-2}$, which is associated with flows with energetic submesoscale currents (Capet et al. 2008a) and white horizontal gradient spectra. The EKE spectral slope found is similar to observations in adjacent regions such as the Southern California Current (Chereskin et al. 2019), which attributes the behavior to an energetic submesoscale and relatively weaker mesoscale than in western boundary currents. Vorticity ζ and divergence δ spectra are proportional to the horizontal velocity gradient, which indicates sharp velocity gradients commonly observed in submesoscale fronts and filaments (Barkan et al. 2019). Figure 4b indicates weaker velocity gradients in the FULL experiment compared to the SMTM case.

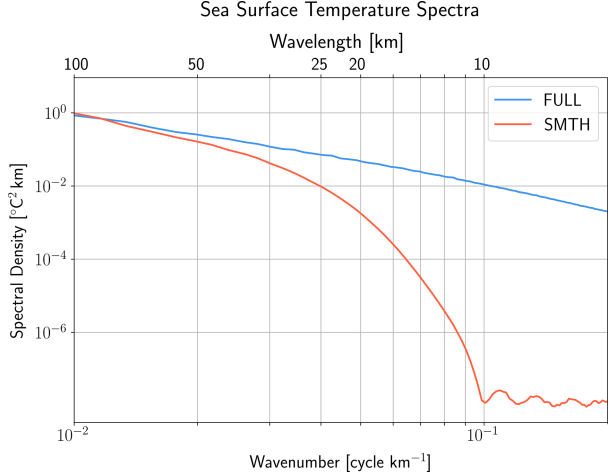


FIG. 3. Isotropic wavenumber spectra comparing the SST fields strictly used for the coupling computation of the model simulation setups FULL and SMTM.

b. EPE flux at the submesoscale

SST anomalies at the submesoscale enhance the loss of APE via correlations between the thermal component of the surface buoyancy flux and the reference level z_r of buoyancy anomalies (which tends to be deeper for cold anomalies and shallower for warm anomalies). Similar effects also hold for the approximate form of the APE flux—EPE as described in (2)—where EPE is lost due to correlations between surface buoyancy anomalies and heat fluxes. A schematic representation of the mechanism above is shown in Fig. 5, where spatial anomalies of buoyancy b' and buoyancy flux B'_o are correlated. The heat flux anomalies respond to SST anomalies at the front to diminish the differences in temperature between the surface ocean and the atmosphere. This mechanism decreases the absolute values of b' and hence the mixed-layer EPE (assuming temperature anomalies and buoyancy anomalies are of the same sign, discussed further in section 5).

The air-sea buoyancy flux B_o may be parameterized as proportional to heat and freshwater fluxes (Cronin and Sprintall 2001):

$$B_o = \frac{\alpha_\theta g}{\rho_o C_p} Q_{\text{net}} - \beta_S g S_o (E - P), \quad (9)$$

where g is the gravity, S_o is the surface salinity, C_p is the specific heat of water, Q_{net} is the net surface heat flux, E is the evaporation, and P is the precipitation. The α_θ and β_S represent the thermal expansion and salinity contraction coefficients calculated at each point. This parameterization allows for the computation of G_{EPE} .

The spectra of G_{APE} and G_{EPE} are shown in Fig. 6. The loss or gain of each to the ocean is represented as negative and positive spectral density values, respectively. Both the APE flux and the approximate form, the EPE flux, show differences exceeding an order of magnitude between the SMTM and FULL experiments. The FULL experiment spectrum shows loss of APE/EPE in the submesoscale and lower mesoscale spatial

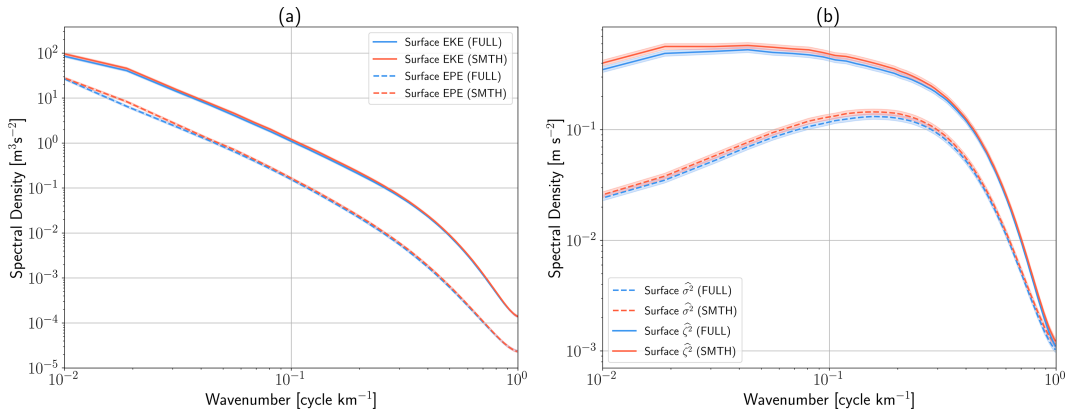


FIG. 4. Surface dynamics and energetics are influenced by air-sea fluxes at the submesoscale. (a) The two-dimensional spectra of surface EKE, in solid lines, and the linear approximation of the APE—the EPE—in dashed lines. (b) Surface vorticity ζ in solid lines and divergence σ in dashed lines. The shading in each spectrum represents the 95% confidence interval calculated from χ^2 distribution using the total number of inertial periods of the experiment's time period as the degrees of freedom. The FULL and SMTH experiments are shown in blue and orange, respectively.

range, which indicates that submesoscale APE/EPE flux acts as a sink of energy to the atmosphere, similar to results found for mesoscale SST anomalies (von Storch et al. 2012; Bishop et al. 2020; Guo et al. 2022; Renault et al. 2023). Conversely, the SMTH experiment spectrum indicates a smaller loss of both APE/EPE compared to the FULL experiment. These differences in surface energy fluxes between the numerical experiments indicate that submesoscale SST variability and the

associated air-sea buoyancy fluxes act to create a sink of submesoscale APE. It is relevant to highlight the differences between the two formulations of APE flux. Although the EPE flux effectively captures the variability and sign of energy flux, as depicted in Fig. 6b, the approximation may overestimate the potential energy flux, especially around the submesoscale range.

c. Decomposition of eddy potential energy flux and approximations

It is useful to understand the contributions of temperature and salinity variability and fluxes to the total flux of APE. This is not straightforward for the exact form of the APE, so here we focus on the EPE, expanding G_{EPE} to assess the importance of each component contributing to b and B_o anomalies. To do this, we first approximate the surface buoyancy into a linear equation that takes into account SST and salinity anomalies and surface values of α_θ and β_S . The linearized surface buoyancy in spectral space is

$$\widehat{b_o} - \widehat{b_{r_o}} \approx g[\widehat{\alpha_\theta \Delta T_o} - \widehat{\beta_S \Delta S_o}], \quad (10)$$

where $\Delta T_o = T_o - T_{r_o}$ and $\Delta S_o = S_o - S_{r_o}$ are the surface temperature and salinity differences with respect to the reference state.

Using (10) and (9), the EPE flux can be divided into components driven by thermal and salinity anomalies and fluxes. This decomposition allows for the assessment of the relative contributions of surface temperature and salinity anomalies and fluxes of heat and freshwater in G_{EPE} . The expansion can be written as

$$G_{\text{EPE}} \approx \frac{1}{N_r^2} \mathbb{R}[\widehat{b_T}^* \widehat{B_{oT}} + \widehat{b_T}^* \widehat{B_{oS}} + \widehat{b_S}^* \widehat{B_{oS}} + \widehat{b_S}^* \widehat{B_{oT}}], \quad (11)$$

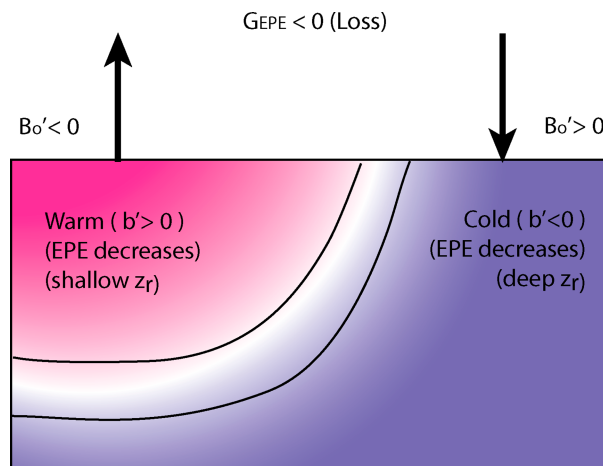


FIG. 5. Schematic representation of the surface flux of EPE driven by SST anomalies and heat flux in a submesoscale front. For simplicity, the buoyancy and buoyancy flux considered in the schematic are treated as due only to the spatial anomalies in SST and heat flux (salinity contributions are discussed in section 4c). Heat flux counteracts the SST anomalies, resulting in a decrease in buoyancy anomaly on both sides of the front and an overall loss of EPE. This concept can also be applied to the water parcel displacements relative to the surface z_r in both sections of the front. The prime symbol represents the spatial anomalies due to the front as in (B1).

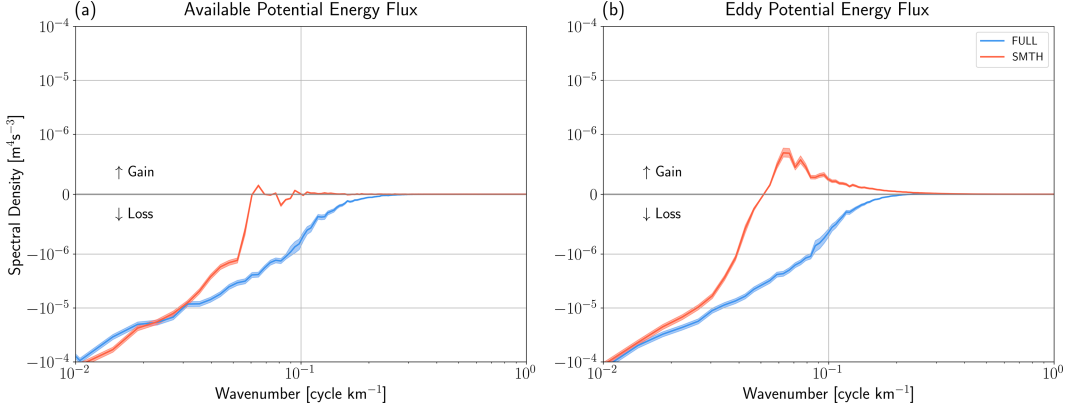


FIG. 6. Submesoscale buoyancy anomalies are correlated with buoyancy flux anomalies, driving a loss of EPE (APE) to the atmosphere. Two-dimensional spectra of APE flux for the FULL (blue line) and SMTM (orange line) experiments. (a) The complete computation of the APE flux based on Zemskova et al. (2015) and Hogg et al. (2013). (b) The approximated formulation of APE flux: EPE flux. The EPE flux spectra show similar variability as the complete formulation of APE flux for the two experiments. The spectra are averaged over the time period of the simulations. Positive (negative) values represent the gain (loss) of EPE in the ocean. The 95% confidence intervals are represented in the shaded areas.

where the components of buoyancy and buoyancy flux are defined as follows:

$$\widehat{b}_T = g\alpha_{\theta}\widehat{\Delta T}_o, \quad (12)$$

$$\widehat{b}_S = -g\beta_S\widehat{\Delta S}_o, \quad (13)$$

$$\widehat{B}_{oT} = \frac{g}{\rho_o C_p} \alpha_{\theta} \widehat{Q}_{\text{net}}, \quad (14)$$

$$\widehat{B}_{oS} = -g\beta_S(E - P)\widehat{S}_o. \quad (15)$$

The total EPE flux thus consists of components from 1) direct correlations between surface temperature anomalies and heat fluxes and surface salinity anomalies and freshwater fluxes and 2) cross terms that arise from the correlations between surface heat fluxes (freshwater fluxes) and salinity anomalies (temperature). The spectra for the four components for the FULL experiments are shown in Fig. 7. The G_{EPE} components related to temperature anomalies (i.e., b_T ; Fig. 7—red lines) indicate a net loss of EPE to the atmosphere, whereas the components generated by salinity anomalies (i.e., b_S ; Fig. 7—blue lines) show a net gain of EPE. The product of the thermal components of buoyancy and buoyancy flux (i.e., $b_T B_{oT}$; Fig. 7—red solid line) is the dominant component of EPE flux to the atmosphere at the submesoscale and is responsible for the net loss of EPE shown in Fig. 6. The term that correlates the salinity component of buoyancy and buoyancy fluxes (i.e., $b_S B_{oS}$; Fig. 7—blue solid line) has the smallest magnitude at the submesoscale, indicating that B_{oS} (proportional to freshwater fluxes) is not as efficient as B_{oT} (proportional to heat fluxes) in injecting EPE in this region. Instead, the component that contributes to the largest gain of EPE in the analysis is the cross-term $b_S B_{oT}$ (Fig. 7—dashed blue line). Temperature and salinity anomalies drive inverse changes in the EPE of the upper ocean, which, as shown below, result from the

partial density compensation of fronts in the California Current region (Rudnick and Ferrari 1999; Mauzole et al. 2020). The B_{oT} may also be further approximated to the latent and sensible components of heat flux anomalies since those are the components correlated to surface buoyancy anomalies. This approximation is useful for scaling the EPE flux mechanism and is explored in the next section.

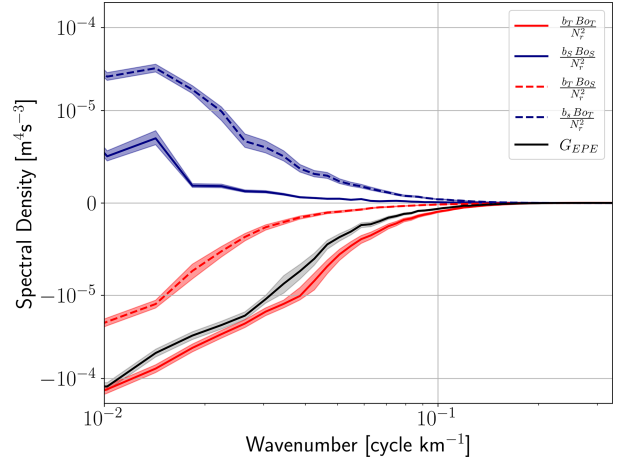


FIG. 7. Decomposition of the total EPE flux (FULL) in terms of the contributions of temperature and salinity components (see section 4c). Blue lines represent the components of G_{EPE} proportional to salinity anomalies b_S . Red lines represent the components proportional to temperature anomalies b_T . The solid blue and red lines represent the components proportional to temperature and heat flux anomalies B_{oT} and to salinity and freshwater flux anomalies B_{oS} . Dashed blue and red lines represent the cross-term components proportional to temperature and freshwater flux anomalies and to salinity and heat flux anomalies, respectively. The black solid line represents the total sum of the components, which accurately explains the total EPE flux term.

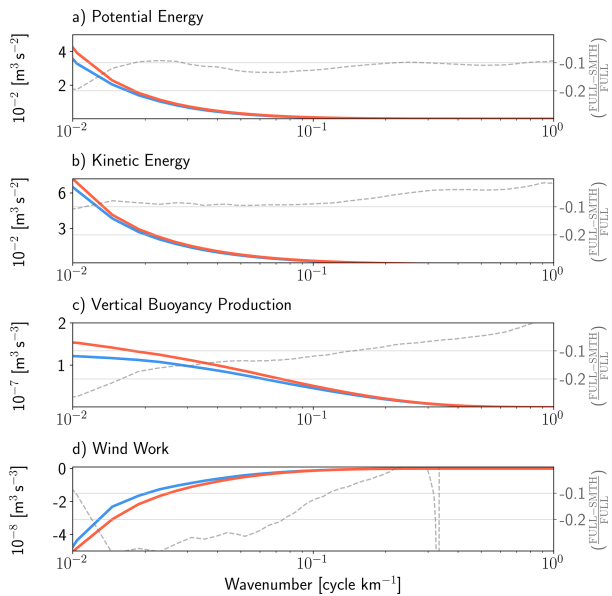


FIG. 8. Cumulative spectra of vertically integrated parameters depict the impact of SST variability in air-sea coupling. Blue (orange) lines represent the FULL (SMTH) experiment spectra. Ogive graphs are integrated from the larger to smaller horizontal wavenumber. (a) Potential energy, (b) kinetic energy, (c) vertical buoyancy production, and (d) wind work. Gray dashed lines indicate the relative difference between the spectra for both experiments. EKE, EPE, and vertical buoyancy production were integrated from 50-m depth to the surface, the averaged mixed-layer depth for the region.

This analysis suggests the EPE flux in these simulations is well approximated by

$$G_{\text{EPE}} \approx \frac{1}{N_r^2} \mathbb{R}[\widehat{b_o}^* \widehat{B}_{oT}]. \quad (16)$$

In the California Current System, the partial *T/S* compensation means that while the thermal component of the buoyancy flux drives a loss of EPE through the temperature anomalies b_T , there is also a partially compensating gain of EPE through the correlation of heat flux anomalies and salinity anomalies b_S . How the EPE flux depends on density compensation more generally is discussed further in section 5 below.

d. Eddy energy reservoirs, conversion rates, and fluxes

Changes in the EPE flux have impacts on the EPE reservoir but can also affect the EKE through the energy conversion terms. The spectra shown in Fig. 4 suggest that, at the surface, the reservoirs of EPE and EKE are both impacted by the response of SST variability in the air-sea energy transfer via EPE flux. The cumulative spectra (or ogives) of the vertically integrated reservoirs of EKE and EPE, averaged over the mixed layer, are shown in Figs. 8a and 8b. The ratios are similar to the ones shown at the surface as in Fig. 4a. For the vertical integration, “ σ ” coordinate is interpolated to “ z ” coordinate to compute the spectra at a fixed depth and equidistant resolution. The mixed-layer depths were obtained by a density threshold of

0.125 kg m⁻³ difference from the surface, and the averaged value of 50 m was used as the integration bound. The EPE flux drives a sink of EPE to the atmosphere due to SST-induced heat flux anomalies (Fig. 6), which generates a reduction of submesoscale EPE in the mixed layer of 10%–20% (Fig. 8a). At the same scales, EKE is also reduced by approximately 10% as seen in Fig. 8b. The EKE reservoir is likely reduced by the smaller rate of eddy energy conversion, namely, vertical buoyancy production [$C_{(\text{EPE}, \text{EKE})}$], which decreases significantly (10%–25%) in the FULL experiment. As mentioned in section 2, $C_{(\text{EPE}, \text{EKE})}$ may be attributed to mixed-layer instabilities (and other ageostrophic secondary circulations), where available potential energy stored in thermal-wind-balanced fronts is extracted and converted into perturbation flows such as eddies (Capet et al. 2008a; Fox-Kemper et al. 2008) again reflecting the weaker submesoscale in FULL versus SMTH (Fig. 4). This comparative analysis indicates that at the submesoscale, G_{EPE} directly reduces the EPE, which induces a lower baroclinic conversion rate [$C_{(\text{EKE}, \text{EPE})}$] and, consequently, results in a decrease in the EKE reservoir in the mixed layer.

Figure 8d also depicts the cumulative difference in surface EKE flux (G_{EKE}) between the two models. Loss of EKE is present in both experiments at the submesoscale since the CFB effect is accounted for in the wind stress parameterizations. At the submesoscale, there is a relative decrease in wind work in the FULL experiment of 15%–30%, a reduction of the EKE flux driven by SST variability. The ratio between the two wind work spectra shown is approximately one or greater than one at scales smaller than the effective resolution of the simulation (approximately 3 km as can be inferred from the rolloff of the EKE spectra in Fig. 4), and hence these scales are not considered in this analysis. Scalings of the CFB mechanism on the wind work indicate a direct relationship between EKE flux and EKE reservoir in the upper ocean (Renault et al. 2017), which is consistent with the decrease of wind work observed in the less energetic FULL experiment (section 5). Concurrently, the TFB mechanism may induce wind anomalies that are partly correlated with surface currents and hence decrease the net loss of EKE by wind work at the submesoscale (Renault et al. 2018; Bai et al. 2023; Conejero et al. 2024; Holmes et al. 2024). This suggests that the more negative wind work in SMTH experiment is likely due to a combination of the artificial suppression of TFB and the increase of surface EKE due indirectly to the suppressed EPE flux.

A simplified Lorenz diagram summarizing the relative differences in energetics between the two experiments is depicted in Fig. 9. The vertically integrated energy fluxes, conversion rates, and reservoirs of both experiments indicate that there is a loss of submesoscale eddy energy in the upper ocean due to correlations between surface buoyancy anomalies and buoyancy fluxes (Fig. 5). This reduction of EPE then decreases the EKE indirectly through a reduction in the conversion of EPE to EKE by vertical buoyancy production. Finally, the reduced EKE is associated with a reduction of CFB wind work, which acts at a rate proportional to the EKE (see section 5). While the magnitude of these changes in the experiments utilized here is relatively small, $\mathcal{O}(10\%)$, they are similar to changes in the energetics caused by the CFB mechanism found in prior

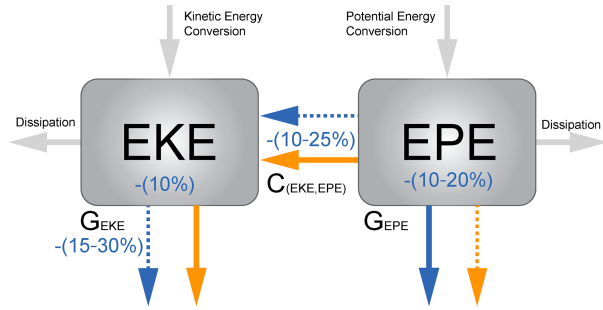


FIG. 9. SST variability at the submesoscale alters the pathways and reservoirs of eddy energy. Simplified Lorenz diagram of the differences in eddy energy reservoirs, fluxes, and conversions. The FULL (SMTH) experiment is illustrated in blue (orange). Differences between the experiments in each component are depicted in terms of the FULL spectra decrease. Fluxes of EPE (i.e., G_{EPE}) and EKE (i.e., G_{EKE}) are represented by the downward arrows. The reservoirs of EPE and EKE are represented by the gray boxes. The conversion of EKE to EPE (i.e., $C_{EPE,EKE}$) is represented by the horizontal arrows. Gray arrows represent the cross-scale conversions and dissipation components of energy that are not the focus of this work.

work in this region (Renault et al. 2018). We discuss the relative importance of these two mechanisms and the role of temperature and salinity variability and compensation in the following section.

5. Discussion

In this work, the surface flux of APE is described at the submesoscale, where it facilitates the transfer of energy between the ocean and the atmosphere via correlations between the surface buoyancy flux and the reference level of the surface buoyancy in the adiabatically resorted background profile. Similar is true for the EPE flux which arises from correlations between the surface buoyancy and surface buoyancy fluxes. This mechanism is previously observed using mesoscale-resolving numerical simulations as described in Ma et al. (2016), Bishop et al. (2017), Guo et al. (2022), and Renault et al. (2023), which affect the energy pathways related to conversion rates and reservoirs of eddy energy. The mechanism described in this work highlights the importance of submesoscale SST variability in driving air-sea fluxes at the same scales and how that may affect the estimation of energy conversion rates, sinks, and reservoirs when using numerical simulations. In this section, the limitations of reproducing the EPE flux in numerical models and the importance of this mechanism relative to other air-sea feedbacks are discussed.

A hierarchy of coupling parameterizations is used in numerical models to reproduce the air-sea fluxes; however, some of the strategies may underestimate or even fail to generate surface EPE fluxes. Coupled numerical simulations that use a responsive atmosphere and bulk formulas to reproduce air-sea fluxes that rely on similarity theory (Monin and Obukhov 1954) can reproduce the mechanism studied in this work (e.g., the FULL simulation). Uncoupled models that use a fixed atmosphere but

calculate heat fluxes using parameterizations that depend on SST will likewise generate EPE fluxes; however, it is possible that this flux may not be entirely accurate as the atmosphere cannot evolve in response to these fluxes. However, uncoupled models that use prescribed heat fluxes (a common approach for regional ocean or idealized numerical simulations) fail to generate the mechanism since surface buoyancy fluxes will not respond to surface buoyancy anomalies. In this case, it is anticipated that the modeled submesoscale will be overly energetic (section 4).

One of the approximation strategies for air-sea fluxes used in uncoupled ocean-only models relies on the linearization of parameters, such as heat flux, into climatological (background) and local anomaly (perturbation) components. The climatological components in the heat flux can then be prescribed based on available data or reanalyses, whereas the heat flux anomalies are parameterized as proportional to modeled surface temperature anomalies (Barnier et al. 1995; Ma et al. 2016; Moreton et al. 2021). This linearization is particularly amenable to simple implementation in ocean-only models and may provide a simpler diagnosis of the impact of SST anomalies on the EPE flux. Here, approximations of the heat flux anomaly as a function of SST are obtained in this region at the submesoscale. This linearization of the heat flux anomaly as proportional to the SST anomaly then allows for a further approximation of the EPE flux mechanism, described below.

For the California Current region, the SST anomalies are mostly correlated to latent and sensible heat flux anomalies at the submesoscale, explaining over 50% of the variance of those heat flux components. This allows for the approximation

$$Q'_{\text{net}} \approx -(Q'_{\text{SH}} + Q'_{\text{LH}}), \quad (17)$$

where Q'_{SH} and Q'_{LH} are the sensible and latent heat flux components, respectively. The approximation has a negative sign since these turbulent heat flux components are subtracted from the shortwave heat flux in Q_{net} computation. The spatial anomalies ('') obtained in this analysis are computed from the subtraction of a spatial low-pass filter, similar to what is applied in the SST field as described in section 3c, to the variable. Figure 10 shows the joint probability distribution for SST and sensible and latent heat flux anomalies over the simulation period. The coupling coefficient α_c is computed as the linear regression fit slope from the approximated heat flux (17) and SST spatial anomalies, as shown in Fig. 10. In this work, $\alpha_c = 31 \text{ W m}^{-2} \text{ }^{\circ}\text{C}^{-1}$, which is similar to previous linearizations for the same region at larger scales (Barnier et al. 1995).

As analyzed in section 4b, the correlation between heat flux and surface buoyancy anomalies has the greatest contribution to the submesoscale EPE flux. By invoking the approximation of EPE flux in physical space (von Storch et al. 2012) and the linearization of the heat flux obtained in this work in (17), an approximate form of the EPE flux is given by

$$G_{\text{EPE}} = -\frac{\alpha_\theta \alpha_c g}{N_r^2 \rho_o C_p} b'_o T'_o. \quad (18)$$

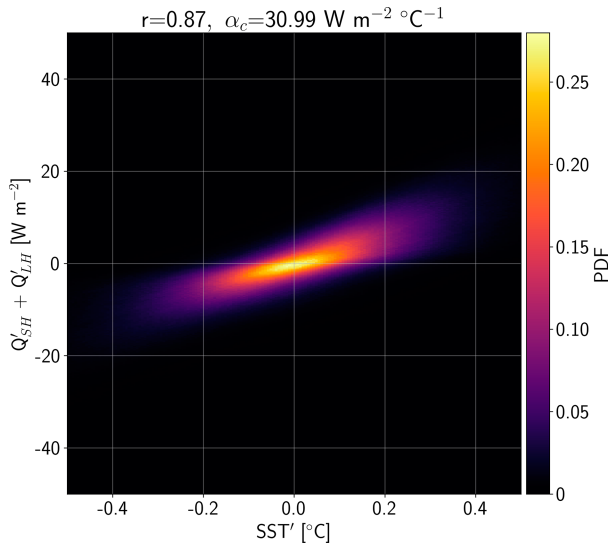


FIG. 10. Two-dimensional histogram of SST and sensible and latent components of the heat flux (Q'_{SH+LH}) anomalies in the FULL simulation setup. The impact of SST anomalies on the EPE flux at the submesoscale may be linearized using a coupling coefficient derived from anomalies of SST and nonsolar heat flux—proportional to surface buoyancy flux.

This approximation describes EPE flux as the product of surface buoyancy and can also be further manipulated by approximating buoyancy by the linear equation of state giving

$$G_{EPE} \approx -\frac{1}{N_r^2} \frac{\alpha_C \alpha_b g^2}{\rho_o C_p} \left(1 - \frac{1}{R}\right) T_o^2, \quad (19)$$

where R is the surface density ratio defined as

$$R = \frac{\alpha_g T_o}{\beta_s S'_o}. \quad (20)$$

This ratio R indicates how temperature and salinity anomalies contribute to the decrease or increase of buoyancy simultaneously. When $R < 0$, the contribution of temperature and salinity anomalies to modulate buoyancy is positively correlated. This scenario favors loss of EPE to the atmosphere as heat flux tends to dissipate buoyancy anomalies (as in Fig. 5), and indeed (19) is strictly negative for $R < 0$. When $R > 0$, the contributions of temperature and salinity anomalies in buoyancy anomalies are negatively correlated; that is, density compensation occurs (Rudnick and Ferrari 1999). Observations suggest some degree of density compensation is ubiquitous in regions with active submesoscales (Rudnick and Martin 2002; Barkan et al. 2017; Drushka et al. 2019). In compensated fronts, the sign of G_{EPE} is dependent on the relative magnitude of the thermal and salinity components of buoyancy in R . If temperature anomalies determine buoyancy anomalies ($R > 1$), then there is a loss of EPE [as in the simulations here where the median value of the ratio $(1 - R^{-1})^{-1} \approx 0.5$]. Conversely, if the salinity component of buoyancy dominates in a compensated front ($0 < R < 1$), such that the surface thermal component of

buoyancy fluxes acts to increase the density anomalies across the front (i.e., the dense side of the front is associated with warm anomalies that are cooled by surface heat fluxes), the EPE will increase due to surface fluxes. This suggests that in some regimes, such as high-latitude β oceans or coastal regions with significant freshwater fluxes, the EPE flux may act as a source of submesoscale energy. This effect has been previously explored in the Gulf of Mexico using realistic simulations, where river outflow has been shown to affect the submesoscale dynamics seasonally (Barkan et al. 2017). In the case of a front approaching complete compensation, $G_{EPE} \rightarrow 0$.

Finally, we note it is also possible to describe G_{EPE} as proportional to the surface EPE reservoir (detailed derivation in appendix B):

$$G_{EPE} \approx \frac{1}{\left(1 - \frac{1}{R}\right)} \frac{2s_b}{\rho_o} EPE_o, \quad (21)$$

where $s_b = -\alpha_C/C_p$ ($\text{kg m}^{-2} \text{s}^{-1}$) is the EPE flux coupling coefficient and EPE_o is the surface EPE. This form is useful for comparison with the CFB EKE flux, which is proportional to EKE (Renault et al. 2017). Although (21) might suggest a singularity as $R \rightarrow 1$, the term $G_{EPE} \rightarrow 0$ since the squared quantity $EPE_o \rightarrow 0$ at a faster rate. The ratio between the two mechanisms can therefore be scaled as

$$\frac{G_{EPE}}{G_{EKE}} \sim \left(\frac{s_b}{s_\tau}\right) \frac{1}{\left(1 - \frac{1}{R}\right)} \frac{EPE_o}{EKE_o}, \quad (22)$$

where $s_\tau = 3/2\rho_a C_D |\mathbf{U}_a|$ is the wind stress coupling coefficient, C_D is the drag coefficient, and $|\mathbf{U}_a|$ is the surface wind magnitude. This ratio indicates that the relative impact between the two mechanisms is a function of (i) the magnitude of both coupling coefficients, (ii) the surface density ratio, and (iii) the ratio of the surface eddy energy reservoirs of the system. The coupling coefficients s_b and s_τ are of similar magnitude considering previous estimates of s_τ using observations (Renault et al. 2017) and of α_c from computations in this work (Fig. 10).

The ratio of EKE_o and EPE_o is scale and season dependent due to mesoscale and submesoscale dynamics. For instance, EKE and EPE spectra of western boundary currents such as the Gulf Stream show that strong baroclinic currents have EKE_o and EPE_o reservoirs of similar magnitude in winter, whereas in summer, EKE is larger (Callies et al. 2015). These differences are in part related to mixed-layer instabilities amplified in wintertime as the mixed-layer depth increases (Fox-Kemper et al. 2008). Observations from the eastern subtropical North Pacific also show EKE and EPE magnitudes to be similar at the mesoscale and submesoscale (Callies and Ferrari 2013). Thus, (22) suggests that the results found here—where the direct EPE flux alters submesoscale energetics in a manner that is quantitatively similar to the surface EKE flux—may be found elsewhere when EPE_o/EKE_o ratio is large or there is substantial density compensation.

6. Summary and conclusions

In this manuscript, the impact of submesoscale SST variability on the flux of EPE is assessed using two configurations of a fully coupled model with submesoscale-permitting resolution in the ocean, where one of the numerical experiments (SMT) suppresses submesoscale SST anomalies in the computation of air-sea fluxes. Comparative analysis between the experiments indicates that modifications to the surface buoyancy flux induced by submesoscale SST variability generate an APE flux at the air-sea interface, which acts as a sink of eddy energy in the upper ocean. In these simulations, this leads to a reduction of the EPE reservoir of 10%–20% at the submesoscale and the small mesoscale. Associated with this, the rate of conversion to EKE by the vertical buoyancy production [$C_{(EPE,EKE)}$] also decreases by 10%–25%. This in turn leads to an approximately 10% reduction of submesoscale EKE and, consequently, a change in the surface wind work (i.e., CFB; Renault et al. 2018) of 15%–30%. These changes to submesoscale energy are similar in magnitude to those induced in the same region by the CFB, as well as at larger scales globally (Renault et al. 2018; Bishop et al. 2020).

Linearizations of the turbulent heat flux as a function of SST perturbations at the submesoscale (coupling coefficient α_c) allow for the scaling of the EPE flux at the submesoscale in terms of surface buoyancy and temperature anomalies. The EPE flux may then be described as a function of the surface EPE, analogous to scaling arguments for EKE flux being proportional to the EKE reservoir (Renault et al. 2017, 2018), with relative magnitude also dependent on the degree of density compensation (Rudnick and Ferrari 1999). A ratio between the EPE and EKE fluxes results in a term proportional to the ratio between the eddy energy reservoirs, suggesting that the relative importance of the EPE flux and CFB mechanisms in reducing eddy energy will be dependent on the relative sizes of the surface EPE and EKE. In this work, considering the California Current region, the EPE flux is a sink of surface EPE at the same magnitude of the CFB mechanism for surface EKE, despite the counteracting effect of the partial salinity compensation found in this region (e.g., Fig. 7). In regions where salinity dominates in the density compensation (e.g., $0 < R < 1$ as found at high latitudes or regions with strong freshwater influence), EPE flux may contribute to a gain of EPE, hence energizing the submesoscale.

We note that changes between simulations at scales larger than the SST filter scale were also observed in these experiments, which could indicate a change in the upscale flux of energy from the submesoscale to the mesoscale. This suggests the possibilities of nonlinear effects not captured in our current interpretation of results (section 4). However, the limited domain size and integration time period of the numerical model considered here do not allow a robust characterization of changes at larger scales. Looking forward, a scale-dependent APE budget study using a submesoscale-resolving experiment in a larger domain would provide useful insight into both the direct and cross-scale effects of the surface energy fluxes and conversion rates. Likewise, extensions of this work to also include additional experiments with spatial filtering of surface

currents, near-surface surface winds, or near-surface atmospheric temperature would provide additional insight into how fine-scale variability on each side of the air-sea interface impacts the energetics and dynamics of the ocean.

Acknowledgments. This work is a contribution to the S-MODE project (Farrar et al. 2025), an EVS-3 Investigation awarded under NASA Research Announcement NNH17ZDA001N-EVS3 and NASA Grants 80NSSC21K0554 and 80NSSC24K0412 awarded under NASA Research Announcement NNH20ZDA001NPO to the University of Maryland, College Park. This work also used the GENCI (project 13051) computing resources and support from I-CASCADE, POSEIDON-SWOT, and M-ODYSEA TOSCA-CNRS projects.

Data availability statement. No observational data were used in this work. Analysis scripts will be made available via <https://github.com/igorchoa/FeedbackSubmeso> upon publication.

APPENDIX A

Available Potential Energy Approximation for Mixed-Layer Submesoscale Dynamics

In this appendix, we first briefly review the origin of the approximate form of the available potential energy (APE) used, and then briefly discuss the validity of that approximation for considering surface APE at the submesoscale in our simulations. The APE describes the portion of potential energy that can be adiabatically converted to kinetic energy. Its definition arises from the volume-conserved subtraction of the total potential energy (i.e., $\rho_0 z b$) and the background potential energy (i.e., $\rho_0 z_r b$), related to the minimum state of energy for the fluid (Winters et al. 1995; Winters and Barkan 2013; Scotti and Passaggia 2019). The buoyancy reference profile and associated displacements are here calculated on every time snapshot of the model with a topography-sensitive single-basin resorting method based on Huang (2005), Tseng and Ferziger (2001), and Stewart et al. (2014).

A local definition of the APE density is given by (Holliday and McIntyre 1981; Roulet and Klein 2009)

$$\text{APE}(z, b) = - \int_{z_r(b)}^z [b - b_r(z')] dz', \quad (\text{A1})$$

which has a volume integral equal to the global APE (Molemaker and McWilliams 2010). Although the local APE is positive definite, it is not quadratic as it includes higher-order terms in its computation.

The approximation of the local APE is given by simplifying the integral of Eq. (A1), assuming small curvature of the reference buoyancy profile b_r over the scales of the water parcel displacements when reordering. It is then approximated as

$$\text{APE}(z, b) \approx -[z - z_r(b)] \frac{[2b - b_r(z) - b_r(z_r)]}{2}. \quad (\text{A2})$$

Since z_r is the inverse mapping of b_r , $b_r(z_r) = b$, and

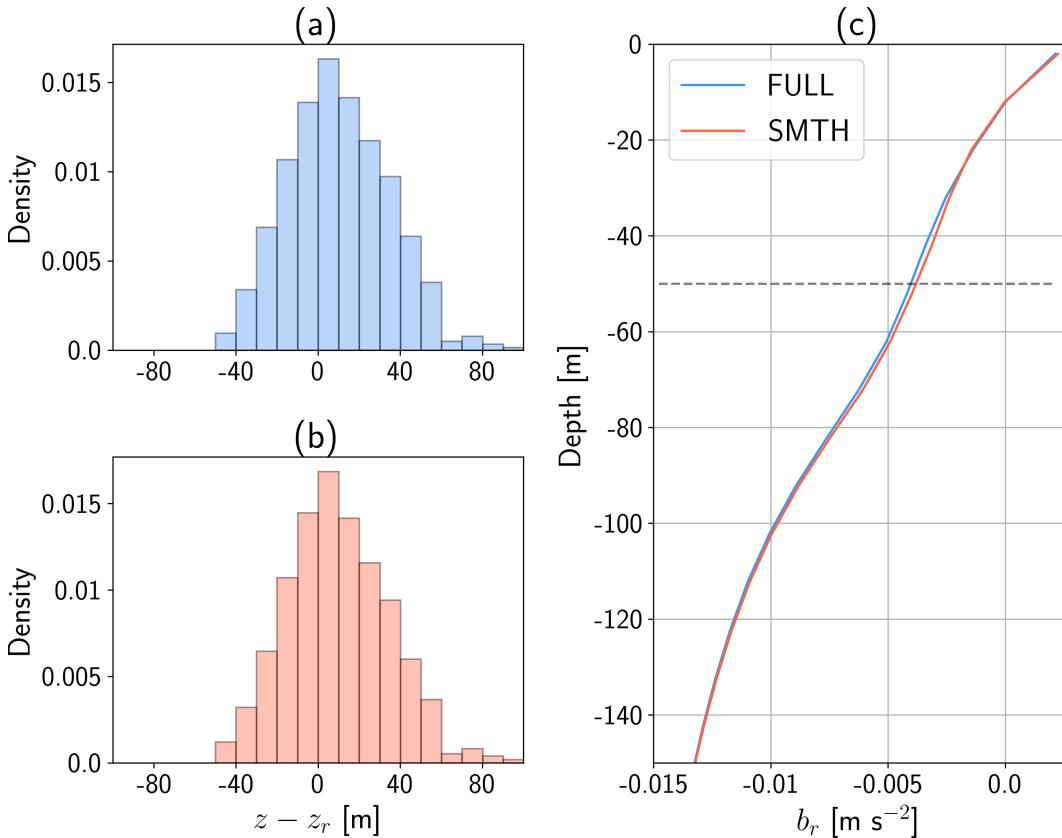


FIG. A1. Small displacements ($z - z_r$) of parcels from their equilibrium height and linear reference density profiles in the mixed layer indicate linear dominance in the local APE density. (a),(b) The histogram of displacements within the averaged mixed-layer depth. (c) The time-averaged reference profile of buoyancy b_r . The gray dashed line represents the averaged mixed-layer depth. Blue colors indicate FULL experiment and red colors indicate SMTM.

$$\text{APE}(z, b) \approx -[z - z_r(b)] \frac{[b - b_r(z)]}{2}. \quad (\text{A3})$$

Linearizing z_r for a fixed b using a first-order Taylor expansion and again assuming the water parcel displacements to be small (Roulet and Klein 2009), z_r becomes

$$z_r(b) \approx z_r(b_r) + [b - b_r] \frac{\partial z_r}{\partial b} \Big|_{b_r}. \quad (\text{A4})$$

By manipulating (A4), an expression for the water parcel displacement for a fixed b is obtained:

$$z - z_r(b) \approx -\frac{(b - b_r)}{N_r^2(z)}. \quad (\text{A5})$$

Applying Eq. (A5) in Eq. (A3) gives the approximate form [which we refer to as the eddy potential energy (EPE) for clarity of terminology]:

$$\text{APE}(z, b) \approx \text{EPE}(z, b) := \frac{[b - b_r]^2}{2N_r^2}. \quad (\text{A6})$$

The APE and EPE are then each also associated with slightly different forms of the surface flux, as discussed in section 2.

This approximation to the APE is common in studies of the submesoscale due to its computational and conceptual simplicity (e.g., Callies and Ferrari 2013; Callies et al. 2015; Cao et al. 2021; Yang et al. 2021). A full assessment of the limitations of the EPE approximation to APE at the submesoscale is beyond the scope of this work; however, we do note that because of the small buoyancy variance at the submesoscale (relative to larger scales), the vertical displacements associated with resorting submesoscale surface buoyancy anomalies are small (Fig. A1). Further, over these depth ranges, the reference buoyancy profile has limited curvature (as opposed to deeper in the permanent pycnocline). Hence, the assumptions used in reaching the EPE (small $z - z_r$, and limited curvature of the reference buoyancy profile) may be reasonable at these scales, at least in the simulation considered here. Regardless, we emphasize that the approximate form is only used in a limited sense in this manuscript: as an approximation for quantifying the “reservoir” of APE in wavenumber space and for determining the relative contributions of salinity and temperature variations and fluxes to the total APE flux. The primary results of the manuscript—submesoscale SST variability inducing fluxes of APE that alter conversion of

APE to EKE and surface wind work—are independent of this approximation.

APPENDIX B

Approximated Form of the EPE Flux at the Submesoscale

The EPE flux is defined as the product of the surface buoyancy and the buoyancy flux anomalies as follows (Bishop et al. 2020; von Storch et al. 2012):

$$G_{\text{EPE}} = \frac{b'_o B'_o}{N_r^2}, \quad (\text{B1})$$

where b'_o and B'_o are defined respectively as

$$b'_o = \alpha_\theta g T'_o - \beta_s g S'_o, \quad (\text{B2})$$

$$B'_o = \frac{\alpha_\theta g}{\rho_o C_p} Q'_{\text{net}} - \beta_s g S'_o [E' - P'], \quad (\text{B3})$$

where the prime symbol ('') denotes the anomaly of a given variable. It is convenient to describe surface buoyancy perturbations in terms of temperature as follows:

$$b'_o = \alpha_\theta g T'_o \left(1 - \frac{1}{R}\right), \quad (\text{B4})$$

where R is the density ratio [defined in (20) and see also Rudnick and Ferrari 1999]. Since at the submesoscale, the EPE flux from the ocean to the atmosphere is primarily generated by surface heat flux anomalies (Fig. 7), we can combine (B4) and (B3) in (B1) to yield

$$G_{\text{EPE}} \approx \frac{1}{N_r^2} \frac{\alpha_\theta^2 g^2}{\rho_o C_p} \left(1 - \frac{1}{R}\right) T'_o Q'_{\text{net}}. \quad (\text{B5})$$

As described in section 5, it is further possible to approximate the correlated component of the heat flux anomaly in terms of a coupling coefficient. The Q'_{net} may then be described as

$$Q'_{\text{net}} \approx -\alpha_C T'_o. \quad (\text{B6})$$

Thus, G_{EPE} is approximately:

$$G_{\text{EPE}} \approx -\frac{1}{N_r^2} \frac{\alpha_C \alpha_\theta^2 g^2}{\rho_o C_p} \left(1 - \frac{1}{R}\right) T'^2_o. \quad (\text{B7})$$

Using the definition of EPE in terms of density ratio:

$$\text{EPE}_o = \frac{1}{2} \frac{\alpha_\theta^2 g^2}{N_r^2} \left(1 - \frac{1}{R}\right)^2 T'^2_o, \quad (\text{B8})$$

and multiplying the term $[1 - (1/R)]$ in the numerator and denominator of (B7), the equation can be manipulated further in terms of b'^2 . Thus, (B7) becomes

$$G_{\text{EPE}} \approx \frac{1}{\left(1 - \frac{1}{R}\right)} \frac{2s_b}{\rho_o} \text{EPE}_o, \quad (\text{B9})$$

where $s_b = -\alpha_C / C_p$ $\text{kg m}^{-2} \text{s}^{-1}$.

This takes a form similar to the current feedback effect on the wind work, which can be expressed as (Renault et al. 2017)

$$G_{\text{EKE}} \approx \frac{2s_\tau}{\rho_o} \text{EKE}_o, \quad (\text{B10})$$

where $s_\tau \approx -3/2\rho_a C_D |\mathbf{U}_a|$ ($\text{kg m}^{-2} \text{s}^{-1}$). Notably, both G_{EPE} and G_{EKE} can thus be seen to act as linear damping terms in the potential and kinetic energy equations, respectively. The ratio between EPE and EKE flux at the submesoscale is

$$\frac{G_{\text{EPE}}}{G_{\text{EKE}}} \sim \frac{2\alpha_C}{3\rho_a C_D C_p |\mathbf{U}_a|} \frac{1}{\left(1 - \frac{1}{R}\right)} \frac{\text{EPE}_o}{\text{EKE}_o}. \quad (\text{B11})$$

REFERENCES

- Bai, Y., A. F. Thompson, A. B. V. Bôas, P. Klein, H. S. Torres, and D. Menemenlis, 2023: Sub-mesoscale wind-front interactions: The combined impact of thermal and current feedback. *Geophys. Res. Lett.*, **50**, e2023GL104807, <https://doi.org/10.1029/2023GL104807>.
- Balwada, D., Q. Xiao, S. Smith, R. Abernathey, and A. R. Gray, 2021: Vertical fluxes conditioned on vorticity and strain reveal submesoscale ventilation. *J. Phys. Oceanogr.*, **51**, 2883–2901, <https://doi.org/10.1175/JPO-D-21-0016.1>.
- Barkan, R., J. C. McWilliams, M. J. Molemaker, J. Choi, K. Srinivasan, A. F. Shchepetkin, and A. Bracco, 2017: Submesoscale dynamics in the northern Gulf of Mexico. Part II: Temperature–salinity relations and cross-shelf transport processes. *J. Phys. Oceanogr.*, **47**, 2347–2360, <https://doi.org/10.1175/JPO-D-17-0040.1>.
- , M. J. Molemaker, K. Srinivasan, J. C. McWilliams, and E. A. D’Asaro, 2019: The role of horizontal divergence in submesoscale frontogenesis. *J. Phys. Oceanogr.*, **49**, 1593–1618, <https://doi.org/10.1175/JPO-D-18-0162.1>.
- Barnier, B., L. Siefridt, and P. Marchesiello, 1995: Thermal forcing for a global ocean circulation model using a three-year climatology of ECMWF analyses. *J. Mar. Syst.*, **6**, 363–380, [https://doi.org/10.1016/0924-7963\(94\)00034-9](https://doi.org/10.1016/0924-7963(94)00034-9).
- Bishop, S. P., R. J. Small, F. O. Bryan, and R. A. Tomas, 2017: Scale dependence of midlatitude air-sea interaction. *J. Climate*, **30**, 8207–8221, <https://doi.org/10.1175/JCLI-D-17-0159.1>.
- , —, and —, 2020: The global sink of available potential energy by mesoscale air-sea interaction. *J. Adv. Model. Earth Syst.*, **12**, e2020MS002118, <https://doi.org/10.1029/2020MS002118>.
- Callies, J., and R. Ferrari, 2013: Interpreting energy and tracer spectra of upper-ocean turbulence in the submesoscale range (1–200 km). *J. Phys. Oceanogr.*, **43**, 2456–2474, <https://doi.org/10.1175/JPO-D-13-063.1>.
- , —, J. M. Klymak, and J. Gula, 2015: Seasonality in submesoscale turbulence. *Nat. Commun.*, **6**, 6862, <https://doi.org/10.1038/ncomms7862>.
- Cao, H., B. Fox-Kemper, and Z. Jing, 2021: Submesoscale eddies in the upper ocean of the Kuroshio Extension from high-resolution simulation: Energy budget. *J. Phys. Oceanogr.*, **51**, 2181–2201, <https://doi.org/10.1175/JPO-D-20-0267.1>.
- Capet, X., J. C. McWilliams, M. J. Molemaker, and A. F. Shchepetkin, 2008a: Mesoscale to submesoscale transition in the California Current system. Part I: Flow structure, eddy flux, and

- observational tests. *J. Phys. Oceanogr.*, **38**, 29–43, <https://doi.org/10.1175/2007JPO3671.1>.
- , —, —, and —, 2008b: Mesoscale to submesoscale transition in the California Current system. Part II: Frontal processes. *J. Phys. Oceanogr.*, **38**, 44–64, <https://doi.org/10.1175/2007JPO3672.1>.
- Chelton, D. B., and S.-P. Xie, 2010: Coupled ocean-atmosphere interaction at oceanic mesoscales. *Oceanography*, **23** (4), 52–69, <https://doi.org/10.5670/oceanog.2010.05>.
- Chereskin, T. K., C. B. Rocha, S. T. Gille, D. Menemenlis, and M. Passaro, 2019: Characterizing the transition from balanced to unbalanced motions in the southern California Current. *J. Geophys. Res. Oceans*, **124**, 2088–2109, <https://doi.org/10.1029/2018JC014583>.
- Conejero, C., L. Renault, F. Desbiolles, J. C. McWilliams, and H. Giordani, 2024: Near-surface atmospheric response to meso- and submesoscale current and thermal feedbacks. *J. Phys. Oceanogr.*, **54**, 823–848, <https://doi.org/10.1175/JPO-D-23-0211.1>.
- Cronin, M. F., and J. Sprintall, 2001: Wind and buoyancy-forced upper ocean. *Encyclopedia of Ocean Sciences*, Elsevier, 3219–3226, <https://doi.org/10.1006/rwos.2001.0157>.
- Debreu, L., P. Marchesiello, P. Penven, and G. Cambon, 2012: Two-way nesting in split-explicit ocean models: Algorithms, implementation and validation. *Ocean Modell.*, **49–50**, 1–21, <https://doi.org/10.1016/j.ocemod.2012.03.003>.
- Drushka, K., W. E. Asher, J. Sprintall, S. T. Gille, and C. Hoang, 2019: Global patterns of submesoscale surface salinity variability. *J. Phys. Oceanogr.*, **49**, 1669–1685, <https://doi.org/10.1175/JPO-D-19-0018.1>.
- Edson, J. B., and Coauthors, 2013: On the exchange of momentum over the open ocean. *J. Phys. Oceanogr.*, **43**, 1589–1610, <https://doi.org/10.1175/JPO-D-12-0173.1>.
- Farrar, J. T., and Coauthors, 2025: S-MODE: The Sub-Mesoscale Ocean Dynamics Experiment. *Bull. Amer. Meteor. Soc.*, **106**, E657–E677, <https://doi.org/10.1175/BAMS-D-23-0178.1>.
- Fox-Kemper, B., R. Ferrari, and R. Hallberg, 2008: Parameterization of mixed layer eddies. Part I: Theory and diagnosis. *J. Phys. Oceanogr.*, **38**, 1145–1165, <https://doi.org/10.1175/2007JPO3792.1>.
- Guo, Y., S. Bishop, F. Bryan, and S. Bachman, 2022: A global diagnosis of eddy potential energy budget in an eddy-permitting ocean model. *J. Phys. Oceanogr.*, **52**, 1731–1748, <https://doi.org/10.1175/JPO-D-22-0029.1>.
- Hogg, A. M., H. A. Dijkstra, and J. A. Saenz, 2013: The energetics of a collapsing meridional overturning circulation. *J. Phys. Oceanogr.*, **43**, 1512–1524, <https://doi.org/10.1175/JPO-D-12-0212.1>.
- Holliday, D., and M. E. McIntyre, 1981: On potential energy density in an incompressible, stratified fluid. *J. Fluid Mech.*, **107**, 221–225, <https://doi.org/10.1017/S0022112081001742>.
- Holmes, R. M., L. Renault, L. Maillard, and J. Boucharel, 2024: Air-sea coupling feedbacks over tropical instability waves. *J. Phys. Oceanogr.*, **54**, 2165–2184, <https://doi.org/10.1175/JPO-D-24-0010.1>.
- Huang, R. X., 2005: Available potential energy in the world's oceans. *J. Mar. Res.*, **63**, 141–158, <https://doi.org/10.1357/0022240053693770>.
- Iyer, S., K. Drushka, E. J. Thompson, and J. Thomson, 2022: Small-scale spatial variations of air-sea heat, moisture, and buoyancy fluxes in the tropical trade winds. *J. Geophys. Res. Oceans*, **127**, e2022JC018972, <https://doi.org/10.1029/2022JC018972>.
- Johnson, L., C. M. Lee, and E. A. D'Asaro, 2016: Global estimates of lateral springtime restratification. *J. Phys. Oceanogr.*, **46**, 1555–1573, <https://doi.org/10.1175/JPO-D-15-0163.1>.
- Jullien, S., S. Masson, V. Oerder, G. Samson, F. Colas, and L. Renault, 2020: Impact of ocean-atmosphere current feedback on ocean mesoscale activity: Regional variations and sensitivity to model resolution. *J. Climate*, **33**, 2585–2602, <https://doi.org/10.1175/JCLI-D-19-0484.1>.
- Large, W. G., J. C. McWilliams, and S. C. Doney, 1994: Oceanic vertical mixing: A review and a model with a nonlocal boundary layer parameterization. *Rev. Geophys.*, **32**, 363–403, <https://doi.org/10.1029/94RG01872>.
- Lorenz, E. N., 1955: Available potential energy and the maintenance of the general circulation. *Tellus*, **7A**, 157–167, <https://doi.org/10.1111/j.2153-3490.1955.tb01148.x>.
- Ma, X., and Coauthors, 2016: Western boundary currents regulated by interaction between ocean eddies and the atmosphere. *Nature*, **535**, 533–537, <https://doi.org/10.1038/nature18640>.
- Mahadevan, A., E. D'Asaro, C. Lee, and M. J. Perry, 2012: Eddy-driven stratification initiates North Atlantic spring phytoplankton blooms. *Science*, **337**, 54–58, <https://doi.org/10.1126/science.1218740>.
- Mauzole, Y., H. S. Torres, and L.-L. Fu, 2020: Patterns and dynamics of SST fronts in the California Current System. *J. Geophys. Res. Oceans*, **125**, e2019JC015499, <https://doi.org/10.1029/2019JC015499>.
- McWilliams, J. C., 2016: Submesoscale currents in the ocean. *Proc. Roy. Soc.*, **472A**, 20160117, <https://doi.org/10.1098/rspa.2016.0117>.
- Molemaker, M. J., and J. C. McWilliams, 2010: Local balance and cross-scale flux of available potential energy. *J. Fluid Mech.*, **645**, 295–314, <https://doi.org/10.1017/S0022112009992643>.
- Monin, A. S., and A. M. Obukhov, 1954: Basic laws of turbulent mixing in the atmosphere near the ground. *Trudy Geofiz. Inst. AN SSSR*, **24**, 163–187.
- Moreton, S., D. Ferreira, M. Roberts, and H. Hewitt, 2021: Air-sea turbulent heat flux feedback over mesoscale eddies. *Geophys. Res. Lett.*, **48**, e2021GL095407, <https://doi.org/10.1029/2021GL095407>.
- Nakanishi, M., and H. Niino, 2006: An improved Mellor–Yamada Level-3 model: Its numerical stability and application to a regional prediction of advection fog. *Bound.-Layer Meteor.*, **119**, 397–407, <https://doi.org/10.1007/s10546-005-9030-8>.
- O'Neill, L. W., D. B. Chelton, and S. K. Esbensen, 2012: Covariability of surface wind and stress responses to sea surface temperature fronts. *J. Climate*, **25**, 5916–5942, <https://doi.org/10.1175/JCLI-D-11-00230.1>.
- Renault, L., C. Deutsch, J. C. McWilliams, H. Frenzel, J.-H. Liang, and F. Colas, 2016: Partial decoupling of primary productivity from upwelling in the California Current system. *Nat. Geosci.*, **9**, 505–508, <https://doi.org/10.1038/ngeo2722>.
- , J. C. McWilliams, and S. Masson, 2017: Satellite observations of imprint of oceanic current on wind stress by air-sea coupling. *Sci. Rep.*, **7**, 17747, <https://doi.org/10.1038/s41598-017-17939-1>.
- , —, and J. Gula, 2018: Dampening of submesoscale currents by air-sea stress coupling in the Californian upwelling system. *Sci. Rep.*, **8**, 13388, <https://doi.org/10.1038/s41598-018-31602-3>.
- , F. Lemarié, and T. Arsouze, 2019: On the implementation and consequences of the oceanic currents feedback in ocean-atmosphere coupled models. *Ocean Modell.*, **141**, 101423, <https://doi.org/10.1016/j.ocemod.2019.101423>.
- , S. Masson, V. Oerder, F. Colas, and J. C. McWilliams, 2023: Modulation of the oceanic mesoscale activity by the

- mesoscale thermal feedback to the atmosphere. *J. Phys. Oceanogr.*, **53**, 1651–1667, <https://doi.org/10.1175/JPO-D-22-0256.1>.
- Roulet, G., and P. Klein, 2009: Available potential energy diagnosis in a direct numerical simulation of rotating stratified turbulence. *J. Fluid Mech.*, **624**, 45–55, <https://doi.org/10.1017/S0022112008004473>.
- Rudnick, D. L., and R. Ferrari, 1999: Compensation of horizontal temperature and salinity gradients in the ocean mixed layer. *Science*, **283**, 526–529, <https://doi.org/10.1126/science.283.5401.526>.
- , and J. P. Martin, 2002: On the horizontal density ratio in the upper ocean. *Dyn. Atmos. Oceans*, **36**, 3–21, [https://doi.org/10.1016/S0377-0265\(02\)00022-2](https://doi.org/10.1016/S0377-0265(02)00022-2).
- Scotti, A., and B. White, 2014: Diagnosing mixing in stratified turbulent flows with a locally defined available potential energy. *J. Fluid Mech.*, **740**, 114–135, <https://doi.org/10.1017/jfm.2013.643>.
- , and P.-Y. Passaggia, 2019: Diagnosing diabatic effects on the available energy of stratified flows in inertial and non-inertial frames. *J. Fluid Mech.*, **861**, 608–642, <https://doi.org/10.1017/jfm.2018.915>.
- Seo, H., A. J. Miller, and J. R. Norris, 2016: Eddy–wind interaction in the California Current System: Dynamics and impacts. *J. Phys. Oceanogr.*, **46**, 439–459, <https://doi.org/10.1175/JPO-D-15-0086.1>.
- , and Coauthors, 2023: Ocean mesoscale and frontal-scale ocean–atmosphere interactions and influence on large-scale climate: A review. *J. Climate*, **36**, 1981–2013, <https://doi.org/10.1175/JCLI-D-21-0982.1>.
- Shao, M., and Coauthors, 2019: The variability of winds and fluxes observed near submesoscale fronts. *J. Geophys. Res. Oceans*, **124**, 7756–7780, <https://doi.org/10.1029/2019JC015236>.
- Shchepetkin, A. F., 2015: An adaptive, Courant-number-dependent implicit scheme for vertical advection in oceanic modeling. *Ocean Modell.*, **91**, 38–69, <https://doi.org/10.1016/j.ocemod.2015.03.006>.
- , and J. C. McWilliams, 2005: The regional oceanic modeling system (ROMS): A split-explicit, free-surface, topography-following-coordinate oceanic model. *Ocean Modell.*, **9**, 347–404, <https://doi.org/10.1016/j.ocemod.2004.08.002>.
- Skamarock, W. C., and Coauthors, 2019: A description of the Advanced Research WRF Model version 4. NCAR Tech. Note NCAR/TN-556+STR, 145 pp., <https://doi.org/10.5065/1dfh-6p97>.
- Skyllingstad, E. D., D. Vickers, L. Mahrt, and R. Samelson, 2007: Effects of mesoscale sea-surface temperature fronts on the marine atmospheric boundary layer. *Bound.-Layer Meteor.*, **123**, 219–237, <https://doi.org/10.1007/s10546-006-9127-8>.
- Small, R. J., and Coauthors, 2008: Air-sea interaction over ocean fronts and eddies. *Dyn. Atmos. Oceans*, **45**, 274–319, <https://doi.org/10.1016/j.dynatmoce.2008.01.001>.
- Stewart, K. D., J. A. Saenz, A. M. Hogg, G. O. Hughes, and R. W. Griffiths, 2014: Effect of topographic barriers on the rates of available potential energy conversion of the oceans. *Ocean Modell.*, **76**, 31–42, <https://doi.org/10.1016/j.ocemod.2014.02.001>.
- Su, Z., J. Wang, P. Klein, A. F. Thompson, and D. Menemenlis, 2018: Ocean submesoscales as a key component of the global heat budget. *Nat. Commun.*, **9**, 775, <https://doi.org/10.1038/s41467-018-02983-w>.
- , H. Torres, P. Klein, A. F. Thompson, L. Siegelman, J. Wang, D. Menemenlis, and C. Hill, 2020: High-frequency submesoscale motions enhance the upward vertical heat transport in the global ocean. *J. Geophys. Res. Oceans*, **125**, e2020JC016544, <https://doi.org/10.1029/2020JC016544>.
- Sullivan, P. P., J. C. McWilliams, J. C. Weil, E. G. Patton, and H. J. S. Fernando, 2020: Marine boundary layers above heterogeneous SST: Across-front winds. *J. Atmos. Sci.*, **77**, 4251–4275, <https://doi.org/10.1175/JAS-D-20-0062.1>.
- , —, —, —, and —, 2021: Marine boundary layers above heterogeneous SST: Alongfront winds. *J. Atmos. Sci.*, **78**, 3297–3315, <https://doi.org/10.1175/JAS-D-21-0072.1>.
- Tseng, Y.-H., and J. H. Ferziger, 2001: Mixing and available potential energy in stratified flows. *Phys. Fluids*, **13**, 1281–1293, <https://doi.org/10.1063/1.1358307>.
- Valek, S., 2013: The OASIS3 coupler: A European climate modelling community software. *Geosci. Model Dev.*, **6**, 373–388, <https://doi.org/10.5194/gmd-6-373-2013>.
- von Storch, J.-S., C. Eden, I. Fast, H. Haak, D. Hernández-Deckers, E. Maier-Reimer, J. Marotzke, and D. Stammer, 2012: An estimate of the Lorenz energy cycle for the world ocean based on the 1/10° STORM/NCEP simulation. *J. Phys. Oceanogr.*, **42**, 2185–2205, <https://doi.org/10.1175/JPO-D-12-0791>.
- Wenegrat, J. O., 2023: The current feedback on stress modifies the Ekman buoyancy flux at fronts. *J. Phys. Oceanogr.*, **53**, 2737–2749, <https://doi.org/10.1175/JPO-D-23-0005.1>.
- , and M. J. McPhaden, 2016: Wind, waves, and fronts: Frictional effects in a generalized Ekman model. *J. Phys. Oceanogr.*, **46**, 371–394, <https://doi.org/10.1175/JPO-D-15-0162.1>.
- , and R. S. Arthur, 2018: Response of the atmospheric boundary layer to submesoscale sea surface temperature fronts. *Geophys. Res. Lett.*, **45**, 13 505–13 512, <https://doi.org/10.1029/2018GL081034>.
- , L. N. Thomas, J. Gula, and J. C. McWilliams, 2018: Effects of the submesoscale on the potential vorticity budget of ocean mode waters. *J. Phys. Oceanogr.*, **48**, 2141–2165, <https://doi.org/10.1175/JPO-D-17-0219.1>.
- Winters, K. B., and R. Barkan, 2013: Available potential energy density for Boussinesq fluid flow. *J. Fluid Mech.*, **714**, 476–488, <https://doi.org/10.1017/jfm.2012.493>.
- , P. N. Lombard, J. J. Riley, and E. A. D’Asaro, 1995: Available potential energy and mixing in density-stratified fluids. *J. Fluid Mech.*, **289**, 115–128, <https://doi.org/10.1017/S002211209500125X>.
- Yang, H., and Coauthors, 2024: Observations reveal intense air-sea exchanges over submesoscale ocean front. *Geophys. Res. Lett.*, **51**, e2023GL106840, <https://doi.org/10.1029/2023GL106840>.
- Yang, Y., J. C. McWilliams, X. S. Liang, H. Zhang, R. H. Weisberg, Y. Liu, and D. Menemenlis, 2021: Spatial and temporal characteristics of the submesoscale energetics in the Gulf of Mexico. *J. Phys. Oceanogr.*, **51**, 475–489, <https://doi.org/10.1175/JPO-D-20-0247.1>.
- Zemskova, V. E., B. L. White, and A. Scotti, 2015: Available potential energy and the general circulation: Partitioning wind, buoyancy forcing, and diapycnal mixing. *J. Phys. Oceanogr.*, **45**, 1510–1531, <https://doi.org/10.1175/JPO-D-14-0043.1>.
- Zhai, X., and R. J. Greatbatch, 2006: Surface eddy diffusivity for heat in a model of the northwest Atlantic Ocean. *Geophys. Res. Lett.*, **33**, L24611, <https://doi.org/10.1029/2006GL028712>.